How to cite: *Angew. Chem. Int. Ed.* **2023**, *62*, e202313940
doi.org/10.1002/anie.202313940

Fluorinated COFs **Hot Paper**

Scalable Synthesis and Electrocatalytic Performance of Highly Fluorinated Covalent Organic Frameworks for Oxygen Reduction

Marcos Martínez-Fernández[+], Emiliano Martínez-Periñán[+], Alejandro de la Peña Ruigómez, Jorge J. Cabrera-Trujillo, Jorge A. R. Navarro, Fernando Aguilar-Galindo, David Rodríguez-San-Miguel, Mar Ramos, Rebecca Vismara, Félix Zamora,* Encarnación Lorenzo,* and José L. Segura**

Abstract: In this study, we present a novel approach for the synthesis of covalent organic frameworks (COFs) that overcomes the common limitations of non-scalable solvothermal procedures. Our method allows for the room-temperature and scalable synthesis of a highly fluorinated DFTAPB-TFTA-COF, which exhibits intrinsic hydrophobicity. We used DFT-based calculations to elucidate the role of the fluorine atoms in enhancing the crystallinity of the material through corrugation effects, resulting in maximized interlayer interactions, as disclosed both from PXRD structural resolution and theoretical simulations. We further investigated the electrocatalytic properties of this material towards the oxygen reduction reaction (ORR). Our results show that the fluorinated COF produces hydrogen peroxide selectively with low overpotential (0.062 V) and high turnover frequency (0.0757 s^{-1}) without the addition of any conductive additives. These values are among the best reported for non-pyrolyzed and metal-free electrocatalysts. Finally, we employed DFT-based calculations to analyse the reaction mechanism, highlighting the crucial role of the fluorine atom in the active site assembly. Our findings shed light on the potential of fluorinated COFs as promising electrocatalysts for the ORR, as well as their potential applications in other fields.

[*] M. Martínez-Fernández,[+] Dr. A. d. l. P. Ruigómez, Prof. J. L. Segura
Facultad de CC. Químicas,
Universidad Complutense de Madrid
Avenida Complutense s/n, 28040 Madrid (Spain)
E-mail: segura@ucm.es

M. Martínez-Fernández,[+] Dr. D. Rodríguez-San-Miguel, Prof. F. Zamora
Departamento de Inorgánica, Facultad de Ciencias,
Universidad Autónoma de Madrid
Campus de Cantoblanco–Crta. Colmenar, 28049 Madrid (Spain)
E-mail: felix.zamora@uam.es

Dr. E. Martínez-Periñán,[+] Prof. E. Lorenzo
Departamento de Química Analítica y Análisis Instrumental,
Facultad de Ciencias, Universidad Autónoma de Madrid
Campus de Cantoblanco–Crta. Colmenar, 28049 Madrid (Spain)
E-mail: encarnacion.lorenzo@uam.es

Dr. E. Martínez-Periñán,[+] Dr. F. Aguilar-Galindo, Dr. D. Rodríguez-San-Miguel, Prof. F. Zamora, Prof. E. Lorenzo
Institute for Advanced Research in Chemical Sciences (IAdChem),
Universidad Autónoma de Madrid
Campus de Cantoblanco, 28049 Madrid (Spain)

Dr. A. d. l. P. Ruigómez, Prof. M. Ramos
Chemical and Environmental Technology Department,
Univ. Rey Juan Carlos
Móstoles, 28933 Madrid (Spain)

Dr. J. J. Cabrera-Trujillo
CNRS/Université de Pau et des Pays de l'Adour E2S-UPPA,
IPREM UMR 5254
64053 Pau Cedex 09 (France)

Prof. J. A. R. Navarro, Dr. R. Vismara
Departamento de Química Inorgánica,
Universidad de Granada
Av. Fuentenueva S/N, 18071 Granada (Spain)
E-mail: rvismara@ugr.es

Dr. F. Aguilar-Galindo
Departamento de Química,
Universidad Autónoma de Madrid
Campus de Cantoblanco–Crta. Colmenar, 28049 Madrid (Spain)

Prof. E. Lorenzo
Instituto Madrileño de Estudios Avanzados en Nanociencia (IMDEA-Nanociencia)
Cantoblanco, 28049 Madrid (Spain)

Prof. F. Zamora
Condensed Matter Physics Center (IFIMAC),
Universidad Autónoma de Madrid
Campus de Cantoblanco, 28049 Madrid (Spain)

[+] These authors contributed equally to this work.

Introduction

In the past decades, emerging porous compounds, such as MOFs, COFs and POPs have revolutionized the field of materials in areas such as adsorption, catalysis, or batteries, since their insoluble and non-fusible character has put it in the spotlight for heterogeneous applications.[1] Furthermore, their large surface areas (in some cases up to 4,000 m^2/g)[2] are highly desirable to avoid the underuse of functional groups, increasing the atomic economy of the final material.[3] Regarding COFs, the possibility of building an organic, crystalline, porous pre-designable structure by the reaction between monomers with modulable properties[4] has attracted enormous attention from scientists over the world. Among all the crystallization methods employed, reversible reaction under solvothermal conditions is usually the most common procedure used.[5] However, this method requires carrying out the reaction in vacuum-sealed Pyrex vessels after freeze-pump-thaw cycles, limiting the amount of synthesised COF.[6] Room-temperature synthesis is one of the most desirable approaches in terms of low energy demand,[7] specially if we consider large-scale production of compounds in its bulk state, such as preparation of oxygen reduction reaction (ORR) electrocatalysts. In this regard, the breakage of the O=O molecule, is an essential and highly efficient process produced in nature.[8] However, to overcome the slow kinetics of the ORR, the assistance of catalyst is necessary to enhance the reaction rates.[9] These electrocatalysts are frequently categorized based on the catalytic pathway: *i*) The direct four-electron pathway reduction of O_2 to H_2O; or *ii*) The two-electron pathway reduction of O_2 to H_2O_2. The two-electron pathway is emerging as a powerful tool to produce on-demand hydrogen peroxide at the consumption site due to the elimination of the transportation cost, the storage requirements and matching the green chemistry principles.[10] To control the ORR pathways, the best performance for the water peroxide production is achieved when the adsorption of the *OOH radical on the electrocatalyst occurs and the adsorption of its dissociation product, the *O radical, is inhibited.[11] In this way, selective control of the ORR pathway can be achieved by controlling the composition of the catalyst, the size, or the electronic structure of the electrocatalyst.[12] Although noble metals still offer the best performances, the scarcity and exorbitant prices of these compounds hinder the utilization of these compounds in commercial devices.[13] One promising alternative for developing ORR electrocatalysts are carbon-based nanomaterials, where non-pyrolyzed and metal-free COFs stand out as promising candidates due to their high stability, low toxicity, high porosity, metal-free composition and crystallinity.[14] The latter feature is very important since it may allow to stablish structural-property relationships to further improve the properties of COF materials for ORR catalysis.[15]

Among all the functionalities introduced, COFs including fluorine atoms in their composition are scarce in the literature despite the interesting properties offered by this highly electronegative atom. Indeed, the fluorinated materials usually display unique properties, such as inversion of the benzene ring charge distribution or increased hydrophobicity.[16] In this way, as shown in Scheme 1, inspired by the multivalency effect found in nature as a key principle to promoting strong and selective interactions,[17] we designed the room-temperature synthesis of a highly-fluorinated DFTAPB-TFTA-COF (DFTAPB = 1,3,5-tris-(2,3,5,6-tetrafluoro)-benzene, and TFTA = 2,3,4,6-tetrafluoroterepthaldehyde) with the following aims: i) expand the record fluorine atom per pore described by Johnson and col.[18] with 24 fluorine atoms per pore by introducing a C_2 unit between the C_3 knots, obtaining a pore with 36 fluorine moieties (Scheme 1); ii) explore their applicability towards ORR electrocatalysis since the polarized sp^2 C–F bond could serve as an active site for O_2 adsorption with high H_2O_2 selectivity in comparison with other fluorinated compounds found in literature;[19] and iii) obtain superhydrophobic cavities to tune the wetting state of the active sites, which have been recently reported as an important factor for gas-consuming processes whose reaction sites are

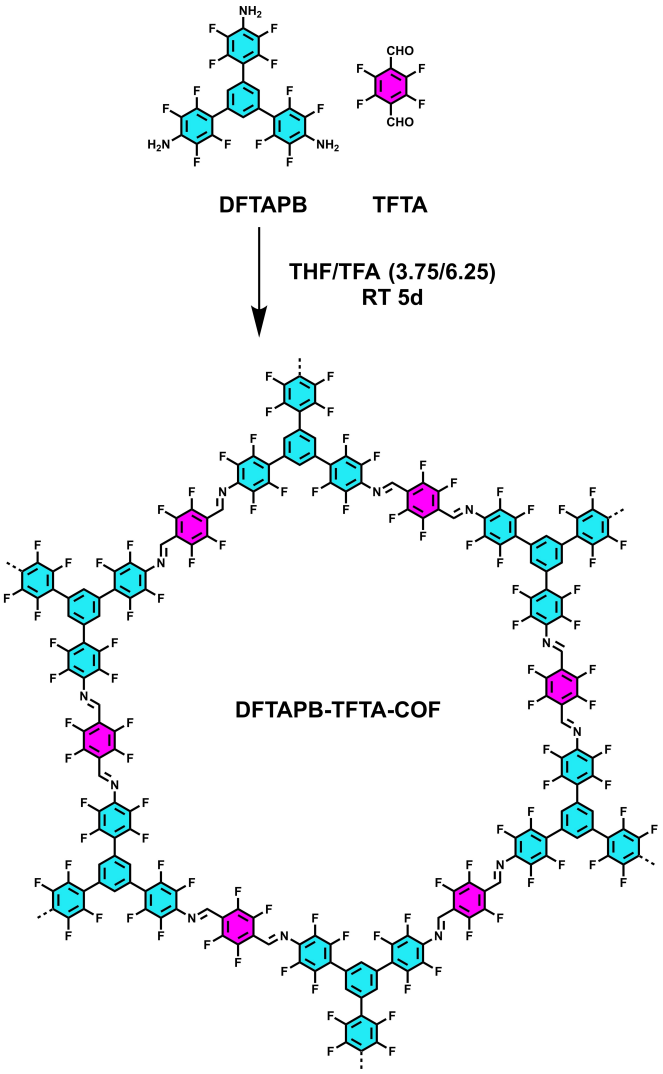

Scheme 1. Scheme of the DFTAPB-TFTA-COF synthesis.

located on a gas/liquid/solid triphasic interface, by the enhancement of the electron transport.[20]

Results and Discussion

DFTAPB-TFTA-COF crystallization was accomplished by Schiff base condensation reaction between the 1,3,5-tris-(2,3,5,6-tetrafluoro)-benzene (DFTAPB) and 2,3,4,6-tetrafluoroterepthaldehyde (TFTA) in a THF/TFA (3.75/6.25) mixture in a glass vial at atmospheric conditions. In this way, following the sol-gel procedure, the monomers were dissolved in THF, and the reaction was triggered by the rapid addition of the TFA (catalyst), producing the rapid gelation of the system (Figure 1A). Finally, the mixture was left standing at 30 °C for 5 days. Remarkably, the crystallization of imine-based COFs usually requires the employment of aqueous acid catalysts to enhance the reticulation processes, the most common aqueous acetic acid. However, the DFTAPB-TFTA-COF could be considered a hydrophobic cavity, as confirmed by the water adsorption isotherm (Figure 1B). The attempts to obtain DFTAPB-TFTA-COF using aqueous acid catalysts yielded no crystalline phases and, in most cases, did not even react. In this way, the water content of the THF and the TFA bottles (*ca.* 0,05 % according to manufacturers), as well as the water produced during the Schiff-base condensation, seems to be enough to promote network curing. Furthermore, no reaction between DFTAPB and TFTA was observed by using acetic acid as a catalyst under similar conditions, suggesting a poorly nucleophilic character of DFTAPB monomer. These facts reveal the challenging nature to achieve highly fluorinated COFs crystallization which are far away from the standard conditions of other networks. Finally, in order to shed light into the properties of the fluorine atom composing the COF skeleton, the isostructural non-fluorinated COF analogue (TAPB-TA-COF) was crystallized by following a room-temperature method described recently by the imine condensation reaction between terephtaldehyde (TA) and 1,3,5-tris(4-aminophenyl)benzene (TAPB) monomers (Scheme 2).[21]

The porosities of both COFs were studied by employing nitrogen sorption isotherms at 77 K (Figure 1C), revealing a type IV isotherm typical of mesoporous materials. Firstly, pore volumes at 0.95 p/p_0 were estimated to be 1.63 $cm^3 g^{-1}$ and 0.65 $cm^3 g^{-1}$ for DFTAPB-TFTA-COF and TAPB-TA-COF, respectively Secondly, the Brunauer–Emmett–Teller (BET) areas were determined to be 1405 $m^2 g^{-1}$ for DFTAPB-TFTA-COF and 926 $m^2 g^{-1}$ for TAPB-TA-COF (Figures S1 and S2, respectively).

The authors would like to emphasize that the surface areas were obtained using low-surface tension solvents (specifically hexane) for COF activation. Although supercritical CO_2 activation would yield more porous networks by

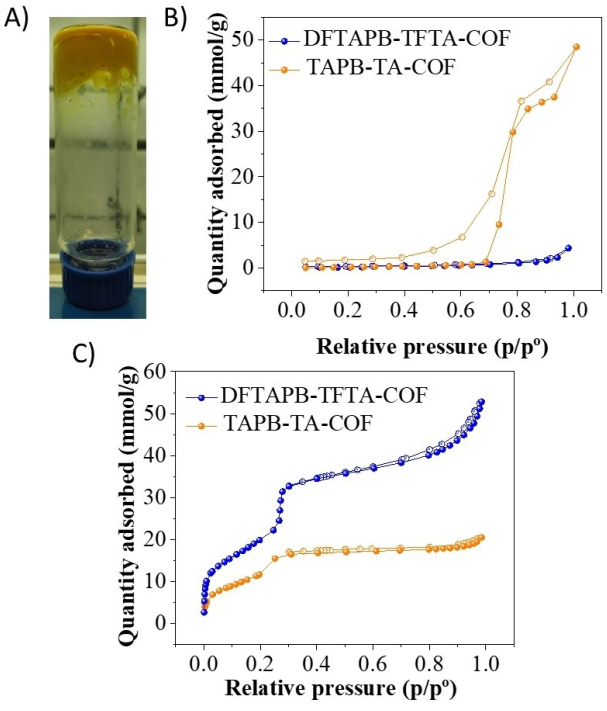

Figure 1. A) Gel phase of the DFTAPB-TFTA-COF. B) Water sorption isotherms at 298 K of DFTAPB-TFTA-COF (blue line) and TAPB-TA-COF (orange line). C) Nitrogen sorption isotherms at 77 K of DFTAPB-TFTA-COF (blue line) and TAPB-TA-COF (orange line). Empty symbols describe the desorption branches.

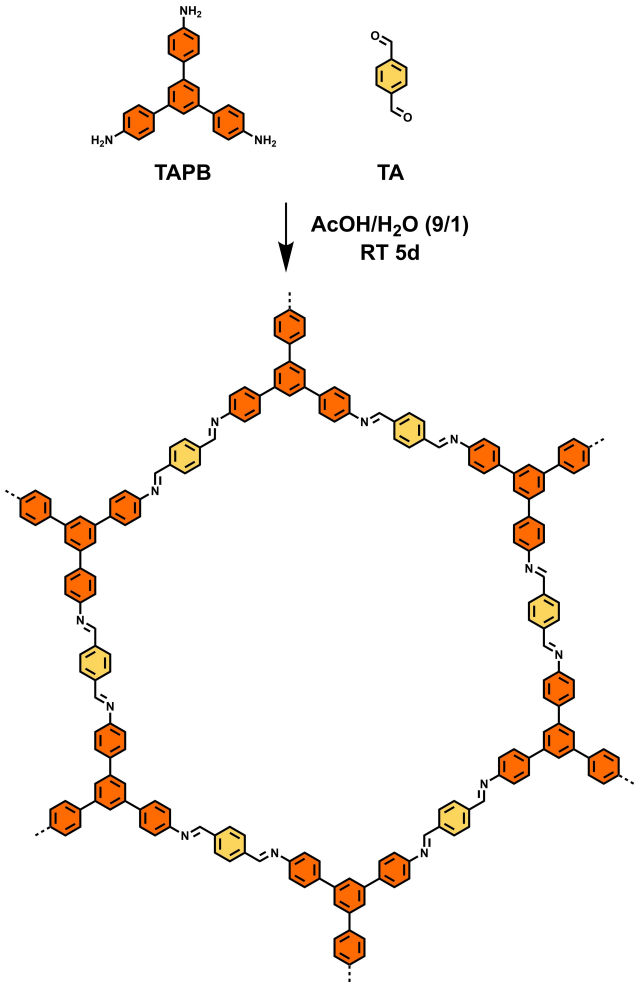

Scheme 2. Scheme of the TAPB-TA-COF synthesis.

avoiding pore collapse, given the non-solvothermal nature of the COFs crystallization, we decided to activate these materials in an open atmosphere to exploit the potential of the scalable method.[22] Finally, non-local density functional theory (NLDFT) was used to calculate the pore size distributions, which were centered at 29 and 27 Å for DFTAPB-TFTA-COF and TAPB-TA-COF, respectively (Figures S3 and S4). These values were contrasted with the theoretical pore volume, surface area and pore opening calculated with Poreblazer V4.0 software being, respectively, 1.069 $cm^3 g^{-1}$, 1361 $m^2 g^{-1}$ and 29 Å for DFTAPB-TFTA-COF, really close to the experimental ones. By contrast, the respective values for TAPB-TA-COF 2.035 $cm^3 g^{-1}$, 2623 $m^2 g^{-1}$ and 31 nm diverge more from the experimental ones, indicating coexistence between amorphous and crystalline domains. The hydrophobicity of the two materials was tested by measuring water adsorption isotherms at 298 K (Figure 1B). As expected, the fluorinated COF is more hydrophobic than the non-fluorinated counterpart. Indeed TAPB-TA-COF, starts to saturate from p/p_0 ~0.7, and shows a hysteresis in the desorption branch, while DFTAPB-TFTA-COF does not saturate in the studied conditions. Furthermore, the hydrophobicity of the materials was also tested with the contact angle of water with the materials (Figure S5), indicating a higher hydrophobic nature of DFTAPB-TFTA-COF (87°) with respect to the non-fluorinated TAPB-TA-COF (74°).

The comparison of the PXRD pattern of DFTAPB-TFTA-COF with that of TAPB-TA-COF suggested that the two COFs are isoreticular[23] (Figure S6). However, up to date, mainly computational models were reported for 2D imine-based COFs, due to their low crystallinity, limited scattering power, and difficulty to be synthesized as single crystals.[24]

Here we propose the preliminary structural characterization of DFTAPB-TFTA-COF starting from PXRD data; the output of the Rietveld refinement can be found in Figure 2A, all the experimental and computational details are reported in the Supporting Information (Figures S7 and S8, and Table S1). DFTAPB-TFTA-COF crystallizes in trigonal symmetry in $P\bar{3}_1c$ space group ($a=b=36.902(4)$ Å, $c=7.336(3)$ Å, $V=8651(3)$ $Å^3$). Its structure is defined by 2-dimensional layers, characterized by hexagonal pores, which stack in AA mode perpendicular to the *c*-axis (Figure 2B-2D and S9). The fluor functionalization of the organic backbone determines a slight torsion between the different 6-membered rings. Namely, 153° around the C2–C3 axis and 182° around the C20–C21 axis, see Figure S10, resulting in a 3.668(1) Å distance between the ring centroids of two adjacent layers, Figure 2E. The unveiled structure shows

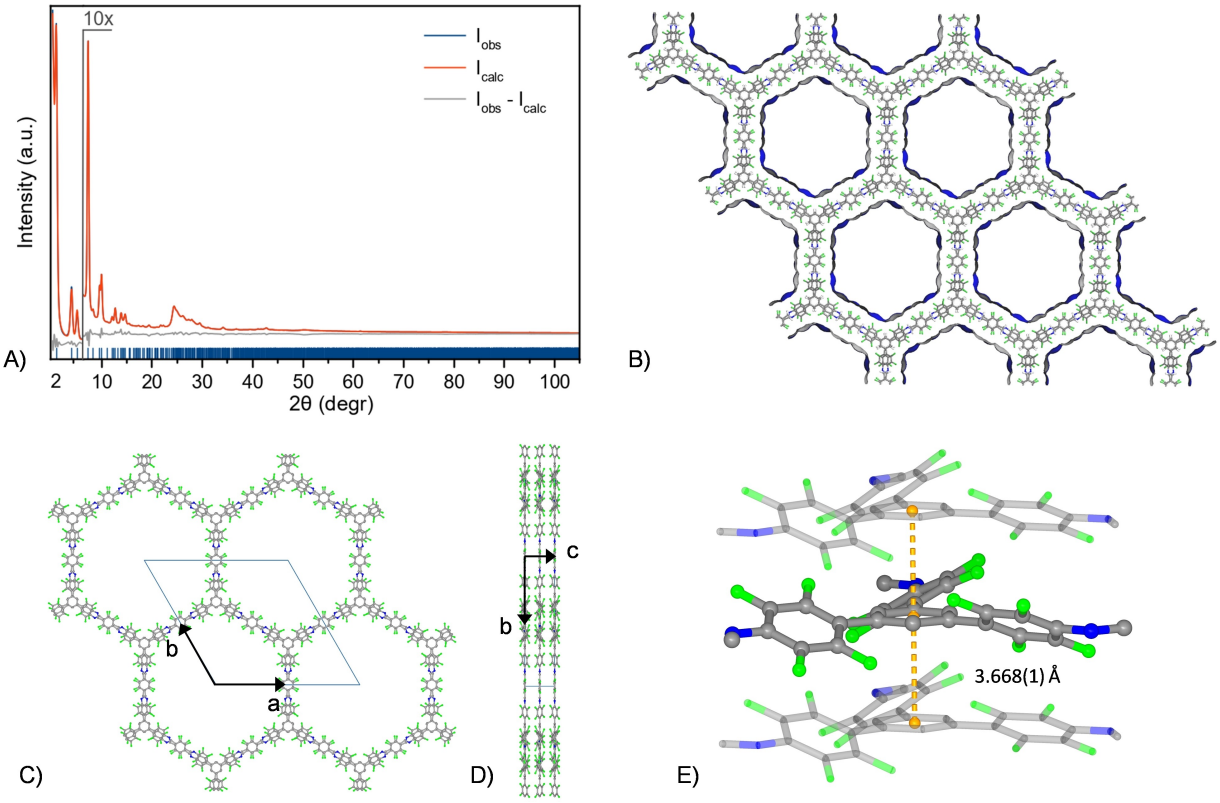

Figure 2. A) Graphical output of the Rietveld refinement of DFTAPB-TFTA-COF. Observed, calculated and difference traces in blue, red and grey respectively. The ticks at the bottom indicate the positions of the Bragg reflection maxima. Figures of merit: $R_p=0.027$, $R_{wp}=0.041$, $R_{Bragg}=0.007$. B) Solvent-accessible surface in DFTAPB-TFTA-COF according to the structural model, viewed along *c*-axis. C) DFTAPB-TFTA-COF structural model as retrieved by Rietveld refinement viewed along *c*-axes and according to *a*-axes (D). E) Distance between the ring centroids of two adjacent layers. Color code: carbon, grey; nitrogen, blue; fluor, green. Hydrogen atoms have been omitted for clarity.

high porosity, ~64.9 % of the unit cell volume,[25] with accessible pores of ~30 Å diameter.

Overall, the experimental structure agrees with the theoretical calculations performed with Density Functional Theory (DFT), including periodicity (see computational details in SI). The simulations predicted similar structures for the two COFs, characterized by the following lattice metrics: $a=b=37.4$ Å, $c=3.8$ Å for TAPB-TA-COF and $a=b=37.4$ Å, $c=3.7$ Å for DFTAPB-TFTA-COF (Figure S11). It is worth noting that the computational unit cell of DFTAPB-TFTA-COF contains one layer, while the experimental one-two; hence the experimental *c*-axis doubles the computed one. On the other hand, the experimental interlayer distance, Figure 2D, perfectly matches the computed *c*-axis (3.668(1) Å *vs* 3.7 Å). Both COFs show corrugation layers, which is higher for DFTAPB-TFTA-COF than for TAPB-TA-COF due to repulsive intralayer F–F interactions, as shown in Figure S11. The corrugation of the structures, also experimentally observed, increases the contact area between the layers, favouring the van der Waals forces. This effect is more pronounced in DFTAPB-TFTA-COF due to the higher corrugation. Therefore, this material will have stronger interlayer interactions and is expected to be more ordered and difficult to exfoliate. We obtained the energy as a function of the *c* value to study the exfoliation, and the results were fitted to a Morse potential. This model predicts an energy cost of ≈14.1 eV/layer for DFTAPB-TFTA-COF *vs* ≈3.5 eV/layer for TAPB-TA-COF (Figure S12). The sorption and diffraction experiments suggest that the degree of order in DFTAPB-TFTA-COF structure is higher than in the non-fluorinated counterpart. This is supported by the analysis of the simulated structures, since the stronger layer-layer interaction in DFTAPB-TFTA-COF helps to fix the atomic positions and the alignment of the layers, thus increasing the material crystallinity. Additionally, theoretical calculations of the formation of the imine bonds in both systems (Figure S13) suggest a lower activation energy for the hydrolysis of the iminium in DFTAPB-TFTA-COF (123.3 kJ mol^{-1}, 1.28 eV) compared to TAPB-TA-COF (146.9 kJ mol^{-1}, 1.52 eV). This greater reversibility could enable faster defect correction in the fluorinated material, enhancing the crystallinity. This fact has also been confirmed experimentally by acid-hydrolytic treatment of the COFs. Upon exposure of the powders to HCl (36 %), complete solution of the fluorine-containing DFTAPB-TFTA-COF was observed, while for the TAPB-TA-COF a black residue was obtained (Figure S14, Supporting Information for details). After treatment of the reaction crude, the diffraction maxima corresponding to the crystalline structures disappeared (Figure S15). However, the residue of DFTAPB-TFTA-COF was soluble in DMSO-d_6 affording the ^{1}H NMR signals (Figure S16) corresponding to the constitutional linkers DFTAPB and TFTA, confirming the higher reversibility of imine bond formation on the fluorinated system in comparison with the non-fluorinated TAPB-TA-COF.

The framework formation was followed by spectrometric techniques such as ^{13}C-cross polarization-magic angle spinning-nuclear magnetic resonance (^{13}C-CP-MAS-NMR) and Fourier-transformed infrared spectroscopy (FTIR). On the one hand, the formation of the imine linkage was confirmed through ^{13}C-CP-MAS-NMR with the disappearance of the aldehyde signals around 180 ppm with the emergence of the imine signal centred at 160 ppm. In addition, the rest of the signals appear between 150–115 ppm, corresponding with the aromatic skeleton of the COFs (Figures S17 and S18), discarding the possibilities of the existence of remaining solvents or catalysts adsorbed in the COF pores. Furthermore, the networks formations were also confirmed by FTIR (Figures S19 and S20) with the fading of the N–H (between 3400–3200 cm^{-1}) and C=O stretch (*ca.* 1685 cm^{-1}) and with the emergence of the imine C=N bands centred at 1622 cm^{-1} for DFTAPB-TFTA-COF and 1619 cm^{-1} for TAPB-TA-COF. Moreover, the intense absorption bands around 1300, 1000, and 900 cm^{-1} were assigned to the aromatic C–F stretching of the DFTAPB-TFTA-COF skeleton by comparison with those found in the bibliography,[26] and with the non-fluorinated TAPB-TA-COF. Furthermore, the thermal stabilities were tested through thermogravimetric analysis (TGA) under a nitrogen atmosphere, revealing that both materials are stable until 450 °C (Figures S21 and S22). Finally, the COFs morphologies were studied through scanning electronic microscopy (SEM) (Figures 3A, 3B, S23, and S24). In this way, SEM images revealed a polygranular composition for both COFs, where each polymer grain is composed of agglomerates of rod-like fibres, which are apparently larger for the TAPB-TA-COF.

To gain insights into the electrocatalytic behaviour of the compounds under study, glassy carbon electrodes were modified with a suspension of DFTAPB-TFTA-COF and TAPB-TA-COF in 20 % ethanol, 0.05 % Nafion in Milli-Q water at 1 mgmL^{-1} concentration (Table 1 summarizes the most relevant results). This mixture was sonicated in an ultrasounds bath at 35 kHz for 30 min and characterized before the electrochemical experiments. The Tyndall effect

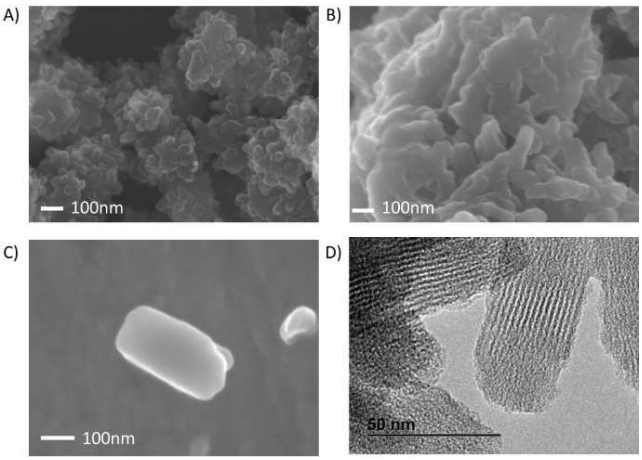

Figure 3. A) SEM image of DFTAPB-TFTA-COF (scale bar 100 nm). B) SEM image of TAPB-TA-COF (scale bar 100 nm). C) SEM image of a rod particle of DFTAPB-TFTA-COF (scale bar 100 nm). D) TEM image of DFTAPB-TFTA-CONs (scale bar 50 nm).

Table 1: Summary of the main electrochemical parameters of **DFTAPB-TFTA-COF** and **TAPB-TA-COF**.

Electrode	E_{onset} vs. SCE [mV]	E_{onset} vs. RHE [mV]	j_{lim} [mA/cm^2]	Tafel Slope [mV/dec]	R_p [kΩ]	TOF [s^{-1}]	Electron number	$\eta_{experimental}$ [V]
DFTAPB-TFTA-COF/GC	−313	+698	−1.70	70.6	4.36	0.0757	2.1	0.062
TAPB-TA-COF/GC	−323	+688	−1.44	119.5	6.64	0.0235	3.3	0.072
GC	−333	+678	−1.18	126.5	6.82	–	2.5	0.082

corroborated the colloidal nature of the obtained suspensions. Then, the as-prepared suspensions were characterized by SEM and transmission electron microscopy (TEM). SEM images revealed rod-like particles for both compounds (Figures 3C and S25). Furthermore, TEM images revealed the thin and highly ordered structure of the COF rods (Figures 3D and S26), which showed average wides of 35 and 30 nm, and average lengths of 82 and 77 nm for DFTAPB-TFTA-COF and TAPB-TA-COF, respectively (Figure S27). Dynamic light scattering (DLS) was employed to study the hydrodynamic diameter of the COF rods in colloidal phase, revealing monomodal distributions, centred at 91 and 256 nm for DFTAPB-TFTA-COF and TAPB-TA-COF, respectively (Figures S28 and S29).

Cyclic voltammetry was employed to characterize the electrochemical behaviour of DFTAPB-TFTA-COF/GC electrodes (0.02 DFTAPB-TFTA-COF mgcm^{-2}). No significant peaks were observed in the absence of oxygen in 0.1 M NaOH (Figure S30), which is ascribed to the absence of electroactive moieties in both COF structures. However, both showed electrocatalytic activity through oxygen reduction in the basic medium (Figure S30). As it is observed, the oxygen reduction peak showed an onset potential of around 25 mV before the onset for ORR of GC electrode and around 20 mV before TAPB-TA-COF/GC (the COF Skeleton without fluorine atoms). Unless the potential shift is not greatly enhanced, the current intensity increases significantly when DFTAPB-TFTA-COF/GC is employed compared with bare GC and TAPB-TA-COF/GC electrodes. In agreement with the results described above, Nyquist plots obtained from Electrochemical Impedance Spectroscopy (EIS) of GC, DFTAPB-TFTA-COF/GC, and TAPB-TA-COF/GC electrodes in O_2 saturated 0.1 M NaOH (Figure S31) clearly show a decrease of charge transfer resistance (Ω) when the GC electrode is modified with any of the COF electrocatalysts, being this decrease more significant when the DFTAPB-TFTA-COF/GC is employed rather than the COF skeleton without fluorine. This points out the role of fluorine atoms in the enhancement of electronic transport, which is essential for high electrocatalytic performances.[20] In order to study COFs conductivity, EIS measurements using a redox probe (($Fe(CN)_6^{4-}$/$Fe(CN)_6^{3-}$) were carried out (Figure S32). As it was expected, when DFTAPB-TFTA-COF and TAPB-TA-COF are deposited on the GC electrode, the non-conductive nature of COF compounds increases the resistance to the electron transfer as deduced from the increase of the radius of the semicircles in the respective Nyquist plots. However, the conductivity of the electrode functionalized with DFTAPB-TFTA-COF is increased in comparison to the halogen-free TAPB-TA-COF, demonstrating the importance of the fluorine functionalization in enhancing electronic conductivity.

Hydrodynamic linear sweep voltammetry using a rotating Pt/CG ring-disc electrode was used to analyse the electrocatalytic behaviour of the polymeric materials towards ORR (Figure 4A). The disk current intensity increases when the GC electrode is modified with COF materials, being higher in the case of the DFTAPB-TFTA-COF/GC. The ring current (applying a constant potential of +0.25 vs SCE, which allows H_2O_2 oxidation) also increases when ORR is happening, being this increase more significant in the case of DFTAPB-TFTA-COF/GC, which agrees well with a higher H_2O_2 generation.

An important point is the number of electrons involved in the ORR process.[11] Figure 4B represents the number of electrons exchanged during ORR, obtaining 2.5 for the bare GC electrode and 3.2 for the TAPB-TA-COF/GC, suggesting the existence of pathway mixtures. Meanwhile, the DFTAPB-TFTA-COF/GC electrode showed a reduction in the electron number at 2.1. This result indicates that the preferable mechanism for ORR is the 2-electron one, characterized by the O_2 reduction into H_2O_2. Calculation of H_2O_2 yield showed the great advantage of DFTAPB-TFTA-COF/GC (96.25 %), compared with GC (78.9 %) and TAPB-TA-COF/GC (44.7 %). The faradaic efficiency (FE_{RRDE}) also showed significant advantages of DFTAPB-TFTA-COF/GC (71.1 %) compared to TAPB-TA-COF/GC (28.7 %) and GC (58.1 %). In addition, Tafel slopes showed a clear decrease when DFTAPB-TFTA-COF is employed as electrocatalyst compared with the bare GC electrode and TAPB-TA-COF/GC (Figure S33), pointing out good electrocatalytic features. Regarding the stability of the DFTAPB-TFTA-COF electrocatalyst, a constant potential of −0.4 V has been applied to a rotating DFTAPB-TFTA-COF/GC disc electrode for 12500 s. As can be observed (Figure 4C), the initial electrocatalytic activity only decreased by less than 10 %, which is a great result, showing the operability of the electrocatalyst for long time in the H_2O_2 presence. The yield rate of H_2O_2 generated during this experiment was measured, using the $Ce(SO_4)_2$ spectrophotometric method, giving a result of 253 mmol/(g_{cat} h). Furthermore, PXRD experiments were performed to analyse the stability of the alkaline media of the electrochemical measurements, revealing the stability of the DFTAPB-TFTA-COF towards the supporting electrolyte (Figure S34). In addition, Raman spectra (Figure S35) and SEM images (Figure S36) were recorded to analyse the possible chemical and morphological changes after the electrocatalytic process.

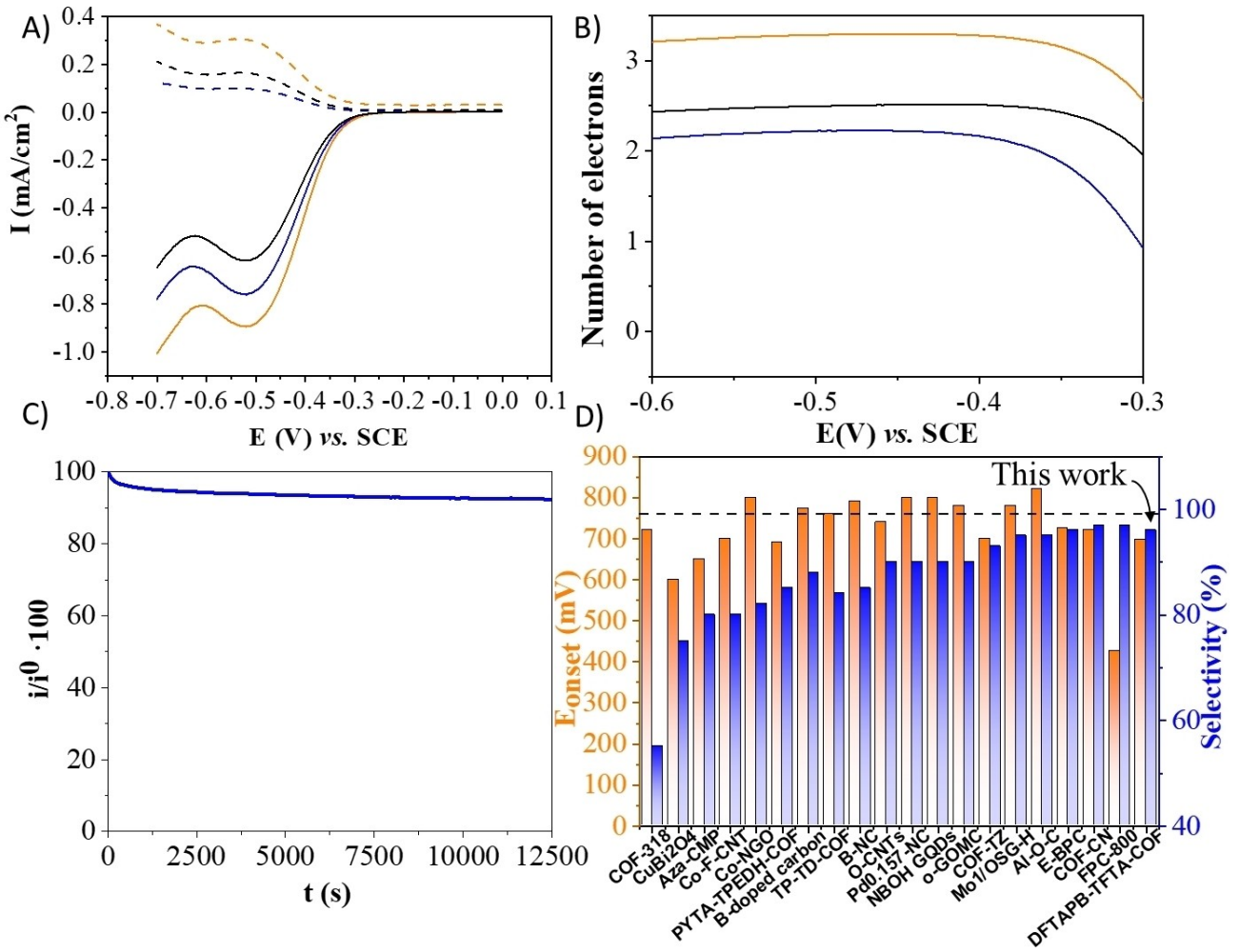

Figure 4. A) Hydrodynamic linear sweep voltammetry of GC (black), TAPB-TA-COF/GC (orange), and DFTAPB-TFTA-COF/GC (blue) in O_2 saturated 0.1 M NaOH solution at 1000 rpm and 10 mV/s. Continuous line disk current and discontinuous line ring current. B) Number of electrons calculated for ORR using RRDE at different potentials. C) Current intensity stability of DFTAPB-TFTA-COF/GC electrode operating in O_2 saturated 0.1 M NaOH solution at a constant potential (−0.4 V vs. SCE). D) E_{onset} vs. RHE (orange, left columns) and Selectivity (blue, right) comparison of DFTAPB-TFTA-COF with the most selective ORR electrocatalysts found in literature (the dotted line represents the thermodynamical equilibrium potential).

The experiments revealed high stability of the developed DFTAPB-TFTA-COF towards the ORR catalysis by observing negligible impact on the chemical structure, crystallinity and materials morphology.

DFTAPB-TFTA-COF displays enhanced properties compared with other COF-based electrocatalysts and is even comparable with other pyrolyzed and/or metallic catalysts regarding potential onset, Tafel slopes, and selectivity. Although some of these catalysts show onset potentials slightly higher than even the thermodynamic limit (attributed to Nerst-related potential change or pH variations due to H_2O_2 generation),[27] the difference is negligible. Therefore, considering the purely organic nature of DFTAPB-TFTA-COF employed without pyrolytic treatments, the total absence of metals (mostly the precious ones), or conductive additives, we can consider DFTAPB-TFTA-COF as excellent electrocatalyst towards the water peroxide generation. In addition, the defined structure apported by the COF platform allows to stablish structural-property relationships,[28] such as the selectivity enhancement by integration of fluorine atoms in a defined sp^2 skeleton as it is demonstrated in the present work. It is worth mentioning that DFTAPB-TFTA-COF outperforms other fluorinated materials including F-doped: carbons,[19b] carbon nanotubes[19c] or transition metal oxides.[29] On the other hand, the crystalline structure of the DFTAPB-TFTA-COF allows the control of the electrocatalyst active sites at atomic-level. This dramatically differs to the atomic structure found in F-doped and pyrolyzed carbons, whose electronic pathway towards ORR varies from 2-electrons[19b,c] to 4-electrons[30] depending on the pyrolytic treatments, the organic precursors used or the fluorine dopant employed. (Figure 4D, Figure S37 and Tables S2 and S3).

To further understand the different electrocatalytic activity showed by the TAPB-TA-COF and the DFTAPB-

TFTA-COF towards the ORR, we carried out Density Functional Theory (DFT) calculations (see ESI for computational details). First, we computed two models (labelled as H-COF and F-COF in Figure 5A) representing the COF structure segment where the active sites are expected to be located. Inspection of the computed electronic structures of these proposed models, reveals that replacing hydrogen with fluorine atoms significantly impacts the frontier molecular orbitals (FMOs) energy. In this sense, HOMO and LUMO are both stabilized (although to different extents) by the presence of fluorine atoms in the F-COF compared to those frontier orbitals in the hydrogenated H-COF (HOMO = −7.79 eV vs −7.21 eV and LUMO = −2.37 eV vs −1.70 eV, respectively, see Figure S38). Remarkably, the computed FMOs produce a lower HOMO–LUMO gap of 5.42 eV for the F-COF compared to this for the H-COF (5.51 eV). These results pointed out that the inclusion of F atoms contributes not only to a stabilization of the FMOs but also to a reduction of the HOMO–LUMO gap, which should be translated into more accessible electronic transfers (Figure S38). This fact is further confirmed by computing the respective adiabatic electron affinity (AEA) for each individual model, i.e., the released energy after the capture of one electron by a neutral COF model to form a radical anion system. We found that F-COF shows an AEA value of −3.5 eV which sharply contrasts with the computed AEA value of −2.8 eV for H-COF. Due to the lower HOMO–LUMO gap and a higher AEA value, fluorinated COF is more prone to capture an electron than the hydrogenated analogous, which aligns with the increased ORR activity.

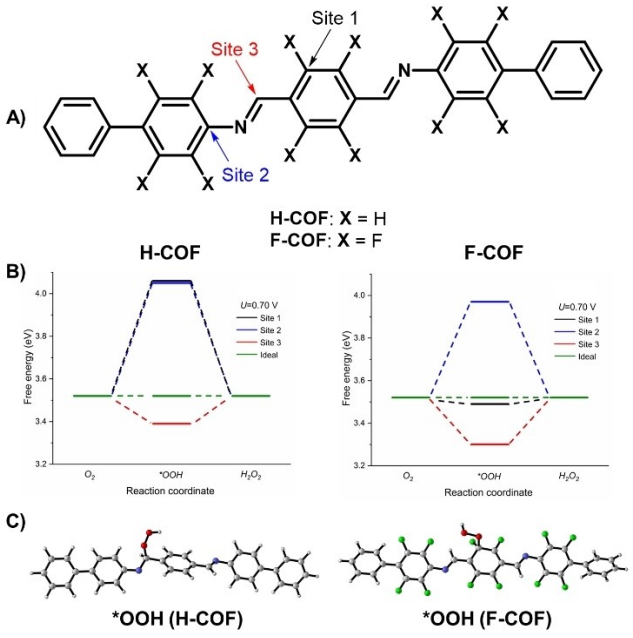

Figure 5. A) Chemical structures for the computed hydrogenated (H-COF) and fluorinated (F-COF) models representing TAPB-TA-COF and DFTAPB-TFTA-COF, respectively. Arrows point to the considered 2e⁻ ORR active sites. B) Computed free energy reaction profiles for the 2e-ORR processes mediated by H-COF (left) or F-COF (right) at three different active sites and electrode potential of 0.70 V. C) DFT-optimized geometries corresponding to the key *OOH intermediates adsorbed on the models H-COF (left) or F-COF (right).

Interestingly, the number of exchanged electrons during the ORR processes has been calculated using RRDE to be ≈3 for the process mediated by the hydrogenated TAPB-TA-COF and ≈2 for the fluorinated DFTAPB-TFTA-COF. Consequently, we proposed that TAPB-TA-COF reduces O_2 to a nearly equivalent mixture of H_2O_2 and H_2O, whereas DFTAPB-TFTA-COF reduces O_2 to H_2O_2 with practically negligible formation of H_2O. To get a deeper insight into this intriguing difference in selectivity, we computationally analysed the 2e⁻ ORR processes mediated by the aforementioned models. To this end, we focused on the most accepted associative mechanism, which involves two elemental steps: (i) Initially, O_2 is reduced to an adsorbed *OOH intermediate ("*" represents the active site in the catalyst surface) and (ii) further reduction of *OOH leads to the release of H_2O_2 (eq. 1–2).

$$O_2(g) + * + (H^+ + e^-) \rightarrow {}^*OOH \quad (1)$$

$$^*OOH + (H^+ + e^-) \rightarrow H_2O_2(I) \quad (2)$$

Based on previous literature, we envisioned three plausible active sites on the catalyst surface (labelled as active sites 1–3 in Figure 5) where the key *OOH intermediate could be formed.[19d,31] The computed reaction profiles of the 2e-ORR mediated by the models H-COF and F-COF are represented in Figure 5B (free energies have been calculated using the computational hydrogen electrode (CHE) model, see ESI for details).[32] Figure 5C depicts the computed optimized geometries for the respective key *OOH intermediates. Noteworthy, the adsorption energy of *OOH intermediates has been proposed as one of the most important activity descriptors for 2e⁻ ORR electrochemical processes.[33] In the processes mediated by the hydrogenated model H-COF, we ruled out active sites 1 and 2 since the formation of intermediates *OOH is uphill and proceeds with high activation barriers of ≈0.55 eV (Figure 5B left). In sharp contrast, when active site 3 is considered, *OOH formation step is downhill (i.e. exothermic), with the subsequent H_2O_2 release now being the limiting step (barrier of 0.13 eV). On the other hand, when examining the processes mediated by the fluorinated model F-COF (Figure 5B right), we found that the favoured pathway is the one involving active site 1. Remarkably, the first step is now downhill, and the subsequent H_2O_2 release step proceeds with a rather low activation barrier of 0.03 eV. These results suggest that the fluorinated DFTAPB-TFTA-COF is not only more electrochemically active (exhibiting a lower activation barrier for a 2e-ORR) than its hydrogenated counterpart TAPB-TA-COF, but also DFTAPB-TFTA-COF displays increased selectivity as the limiting step in both cases is the release of H_2O_2 which is favoured by the fluorinated catalyst.

Once the active site is defined, to compare the intrinsic activities of the electrocatalysts, turnover frequency (TOF) was calculated at 0.5 V vs RHE. As expected, DFTAPB-TFTA-COF showed a larger TOF value of 0.0757 s^{-1} than

TAPB-TA-COF (0.0235 s^{-1}), which is among the best results found in the literature for metal-free and non-pyrolyzed COF-based ORR electrocatalyst through the two-electron pathway (see Table S2). Furthermore, experimental overpotentials were calculated, revealing that the process is near to the equilibrium value with overpotential values of 0.062 V and 0.072 V for DFTAPB-TFTA-COF and TAPB-TA-COF, respectively. The same trend was also found by the DFT-based CHE method with calculated overpotential values of 0.03 V and 0.13 V, respectively.

Motivated by the excellent electrochemical results of DFTAPB-TFTA-COF towards the ORR electrocatalysis and taking advantage of the soft crystallization conditions, we decided to test the scale-up of the reaction by comparing the crystallinity and porosity of the different batches since these two properties are the most prone to be affected at the COF scaling. To address this end, we decided to carry out a 45 mg batch, a 450 mg batch, and a 1023 mg batch, which were named respectively as small, medium, and large batches to simplify. All the systems were reacted following the sol-gel procedure, and the rapid gelation of the system was observed for all the cases, as shown in Supporting Information (video 1). Finally, the reactions were left undisturbed 5 days at 30 °C.

The obtained material quality was assessed by means of PXRD, N_2 adsorption isotherm, and FTIR, see Figure 6. PXRD confirmed that three batches are isostructural and with similar crystallinity (Figure 6A). N_2 sorption isotherms at 77 K revealed a type IV isotherm for all the materials, hence demonstrating that mesoporous nature is retained during the scale-up (Figure 6B). The BET areas fell in the same range (1405, 1131, 1255 $m^2 g^{-1}$ from the small batch to the large one, Figures S1, S39 and S40), and the pore sizes were found around 29 Å for all the materials (Figure 6C). Finally, all the FTIR spectra remained practically identical (Figure 6D), confirming that the COF networks display the same chemical structure. These results suggest that, although the COF crystallization is slightly affected by the scaling, the materials are still presenting great crystalline and porous features, concluding that the novel DFTAPB-TFTA-COF passed the gram-scale production bottleneck satisfactorily (Figure 6E).

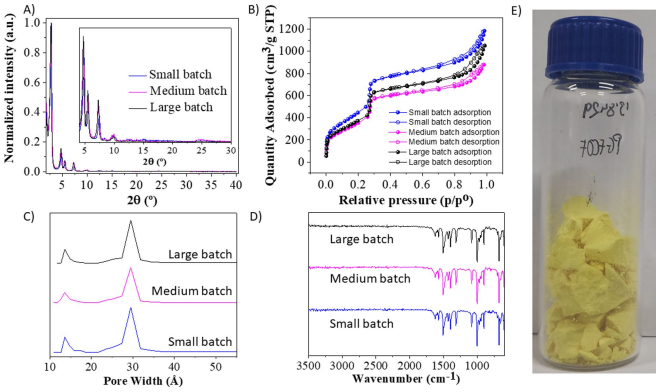

Figure 6. A) Comparison of the PXRD diffractograms of the small (blue trace), medium (pink trace) and large (black trace) DFTAPB-TFTA-COF batches. B) N_2 sorption isotherms at 77 K, empty symbols stand for the desorption branch. C) Pore sizes and D) FTIR spectra of the different batches (blue, pink and black traces refer to small, medium and large batch respectively). E) Photograph of the DFTAPB-TFTA-COF (large batch) amount obtained by the non-solvothermal method.

Conclusion

In the present work, the crystallization of a highly fluorinated DFTAPB-TFTA-COF was reported for the first time and its structure elucidated by PXRD and Theoretical calculations. The effects of the introduction of the fluorine atom in the COF skeleton were studied and compared to the non-fluorinated TAPB-TA-COF counterpart, revealing that the F nucleus favours the interlayers interaction arising in more crystalline and porous structures. Both COFs were tested as ORR electrocatalysts having significant differences in the electronic pathway during the oxygen reduction. Remarkably, the fluorine substitution on DFTAPB-TFTA-COF enhance the selectivity of the electrochemical process towards the hydrogen peroxide generation with 96 % selectivity at near-zero overpotential. DFT-based calculations revealed that the higher electrocatalytic activity of the fluorinated COF compared to its hydrogenated analogous can be rationalized due to greater stabilization of the frontier molecular orbitals, lower HOMO–LUMO gap, and higher adiabatic electron affinity. It is also found that the different ORR selectivity (reduction to H_2O_2 or H_2O) can be understood with a reduction process occurring in different active sites depending on whether the fluorinated or the hydrogenated COF is involved. DFTAPB-TFTA-COF outperforms other fluorine-doped pyrolysis-derived carbonaceous electrocatalysts and presents a comparable performance with other carbon-based active sites, including metalized nanocarbons. The excellent electrocatalytic performance, together with the advantage of the room-temperature and scalable synthesis of the novel DFTAPB-TFTA-COF points out this product as an excellent candidate to on-demand production of H_2O_2 at the consumption sites, eliminating the storage and transportation costs. We envisage the present work revealing valuable information about structural-property relationships in assembling novel electrocatalysts based on non-pyrolyzed and metal-free COFs.

Acknowledgements

This work was financially supported by Ministerio de Ciencia e Innovación of Spain MICINN (TED2021-129886B-C41, TED2021-129886BC42; TED2021-129886BC43; PID2019-106268GB-C32; PID2019-106268GB-C33, PID2020-113608RB-I00; PID2022-138908NB-C33, PID2022-138470NB-100, RED2018-102412-T; PID2020-116728RB-I00). Comunidad de Madrid (P2018/NMT-4349 TRANSNANOAVANSENS Program; SI3/PJI/2021-0034). F.Z. acknowledge financial support from the Spanish Ministry of Science and Innovation, through the "María de Maeztu" Programme for Units of Excellence in R&D

(CEX2018-000805-M). R.V. acknowledges "Programa Juan de la Cierva Formación" (FJC2020-045043-I). R.V. and J.A.R.N. acknowledge MCIN/AEI/10.13039/501100011033 and European Union NextGenerationEU/PRTR.

Conflict of Interest

The authors declare no conflict of interest.

Data Availability Statement

The data that support the findings of this study are available from the corresponding author upon reasonable request.

Keywords: COF · Electrocatalysis · Frameworks · H_2O_2 · ORR

[1] K. Geng, T. He, R. Liu, S. Dalapati, K. T. Tan, Z. Li, S. Tao, Y. Gong, Q. Jiang, D. Jiang, *Chem. Rev.* **2020**, *120*, 8814–8933.
[2] X. Feng, X. Ding, D. Jiang, *Chem. Soc. Rev.* **2012**, *41*, 6010–6022.
[3] C. S. Diercks, O. M. Yaghi, *Science* **2017**, *355*, eaal1585.
[4] J. L. Segura, S. Royuela, M. Mar Ramos, *Chem. Soc. Rev.* **2019**, *48*, 3903–3945.
[5] S. Kandambeth, K. Dey, R. Banerjee, *J. Am. Chem. Soc.* **2019**, *141*, 1807–1822.
[6] a) S. Karak, S. Kandambeth, B. P. Biswal, H. S. Sasmal, S. Kumar, P. Pachfule, R. Banerjee, *J. Am. Chem. Soc.* **2017**, *139*, 1856–1862; b) W. Zhao, L. Xia, X. Liu, *CrystEngComm* **2018**, *20*, 1613–1634.
[7] a) A. R. Bagheri, N. Aramesh, *J. Mater. Sci.* **2021**, *56*, 1116–1132; b) A. de la Peña Ruigómez, D. Rodríguez-San-Miguel, K. C. Stylianou, M. Cavallini, D. Gentili, F. Liscio, S. Milita, O. M. Roscioni, M. L. Ruiz-González, C. Carbonell, D. Maspoch, R. Mas-Ballesté, J. L. Segura, F. Zamora, *Chem. Eur. J.* **2015**, *21*, 10666–10670.
[8] R. Ma, G. Lin, Y. Zhou, Q. Liu, T. Zhang, G. Shan, M. Yang, J. Wang, *npj Comput. Mater.* **2019**, *5*, 78.
[9] D. Grumelli, B. Wurster, S. Stepanow, K. Kern, *Nat. Commun.* **2013**, *4*, 2904.
[10] E. Martínez-Periñán, I. Bravo, S. J. Rowley-Neale, E. Lorenzo, C. E. Banks, *Electroanalysis* **2018**, *30*, 436–444.
[11] Y. Li, J. Chen, Y. Ji, Z. Zhao, W. Cui, X. Sang, Y. Cheng, B. Yang, Z. Li, Q. Zhang, L. Lei, Z. Wen, L. Dai, Y. Hou, *Angew. Chem. Int. Ed.* **2023**, *62*, e202306491.
[12] J. Huang, C. Fu, J. Chen, N. Senthilkumar, X. Peng, Z. Wen, *CCS Chem.* **2022**, *4*, 566–583.
[13] A. A. Gewirth, J. A. Varnell, A. M. DiAscro, *Chem. Rev.* **2018**, *118*, 2313–2339.
[14] Y. Xu, P. Cai, K. Chen, Q. Chen, Z. Wen, L. Chen, *Angew. Chem. Int. Ed.* **2023**, *62*, e202215584.
[15] J. Liu, J. Zhao, C. Li, Y. Liu, D. Li, H. Li, V. Valtchev, S. Qiu, Y. Wang, Q. Fang, *Small* **2023**, *19*, 2305759.
[16] Y. Liu, W. Li, C. Yuan, L. Jia, Y. Liu, A. Huang, Y. Cui, *Angew. Chem. Int. Ed.* **2022**, *61*, e202113348.
[17] R. Haag, *Beilstein J. Org. Chem.* **2015**, *11*, 848–849.
[18] W. A. Braunecker, K. E. Hurst, K. G. Ray, Z. R. Owczarczyk, M. B. Martinez, N. Leick, A. Keuhlen, A. Sellinger, J. C. Johnson, *Cryst. Growth Des.* **2018**, *18*, 4160–4166.
[19] a) Y. Chang, J. Chen, J. Jia, X. Hu, H. Yang, M. Jia, Z. Wen, *Appl. Catal. B* **2021**, *284*, 119721; b) K. Zhao, Y. Su, X. Quan, Y. Liu, S. Chen, H. Yu, *J. Catal.* **2018**, *357*, 118–126; c) S. Zeng, S. Wang, H. Zhuang, B. Lu, C. Li, Y. Wang, G. Wang, *Electrochim. Acta* **2022**, *420*, 140460; d) H. Wang, C. Yang, F. Chen, G. Zheng, Q. Han, *Angew. Chem. Int. Ed.* **2022**, *61*, e202202328.
[20] P. Wang, T. Hayashi, Q. a Meng, Q. Wang, H. Liu, K. Hashimoto, L. Jiang, *Small* **2017**, *13*, 1601250.
[21] J. Á. Martín-Illán, D. Rodríguez-San-Miguel, O. Castillo, G. Beobide, J. Perez-Carvajal, I. Imaz, D. Maspoch, F. Zamora, *Angew. Chem. Int. Ed.* **2021**, *60*, 13969–13977.
[22] D. Zhu, R. Verduzco, *ACS Appl. Mater. Interfaces* **2020**, *12*, 33121–33127.
[23] M. Eddaoudi, J. Kim, N. Rosi, D. Vodak, J. Wachter, M. O'Keeffe, O. M. Yaghi, *Science* **2002**, *295*, 469–472.
[24] a) A. Natraj, W. Ji, J. Xin, I. Castano, D. W. Burke, A. M. Evans, M. J. Strauss, M. Ateia, L. S. Hamachi, N. C. Gianneschi, Z. A. Alothman, J. Sun, K. Yusuf, W. R. Dichtel, *J. Am. Chem. Soc.* **2022**, *144*, 19813–19824; b) T. Ma, E. A. Kapustin, S. X. Yin, L. Liang, Z. Zhou, J. Niu, L.-H. Li, Y. Wang, J. Su, J. Li, X. Wang, W. D. Wang, W. Wang, J. Sun, O. M. Yaghi, *Science* **2018**, *361*, 48–52; c) C. Kang, K. Yang, Z. Zhang, A. K. Usadi, D. C. Calabro, L. S. Baugh, Y. Wang, J. Jiang, X. Zou, Z. Huang, D. Zhao, *Nat. Commun.* **2022**, *13*, 1370.
[25] D. Ongari, A. V. Yakutovich, L. Talirz, B. Smit, *ACS Cent. Sci.* **2019**, *5*, 1663–1675.
[26] L. Chen, J. Du, W. Zhou, H. Shen, L. Tan, C. Zhou, L. Dong, *Chem. Asian J.* **2020**, *15*, 3421–3427.
[27] G. Román-Pérez, J. M. Soler, *Phys. Rev. Lett.* **2009**, *103*, 096102.
[28] a) X. Xu, Y. Gao, Q. Yang, T. Liang, B. Luo, D. Kong, X. Li, L. Zhi, B. Wang, *Nano Today* **2023**, *49*, 101792; b) S. An, X. Li, S. Shang, T. Xu, S. Yang, C.-X. Cui, C. Peng, H. Liu, Q. Xu, Z. Jiang, J. Hu, *Angew. Chem. Int. Ed.* **2023**, *62*, e202218742; c) N. Keller, D. Bessinger, S. Reuter, M. Calik, L. Ascherl, F. C. Hanusch, F. Auras, T. Bein, *J. Am. Chem. Soc.* **2017**, *139*, 8194–8199.
[29] Y. Xu, Z. Li, X. Hu, X. Wu, W. Chen, S. Zhou, J. Li, C. Qi, D.-K. Ma, *J. Catal.* **2022**, *410*, 339–346.
[30] a) X. Sun, Y. Zhang, P. Song, J. Pan, L. Zhuang, W. Xu, W. Xing, *ACS Catal.* **2013**, *3*, 1726–1729; b) X. Sun, P. Song, T. Chen, J. Liu, W. Xu, *Chem. Commun.* **2013**, *49*, 10296–10298; c) X. Zhang, Y. Chen, J. Wang, Q. Zhong, *ChemistrySelect* **2016**, *1*, 696–702; d) S. Jiang, Y. Sun, H. Dai, J. Hu, P. Ni, Y. Wang, Z. Li, Z. Li, *Nanoscale* **2015**, *7*, 10584–10589.
[31] D. Guo, R. Shibuya, C. Akiba, S. Saji, T. Kondo, J. Nakamura, *Science* **2016**, *351*, 361–365.
[32] J. K. Nørskov, J. Rossmeisl, A. Logadottir, L. Lindqvist, J. R. Kitchin, T. Bligaard, H. Jónsson, *J. Phys. Chem. B* **2004**, *108*, 17886–17892.
[33] A. Kulkarni, S. Siahrostami, A. Patel, J. K. Nørskov, *Chem. Rev.* **2018**, *118*, 2302–2312.

Manuscript received: September 18, 2023
Accepted manuscript online: October 16, 2023
Version of record online: October 25, 2023